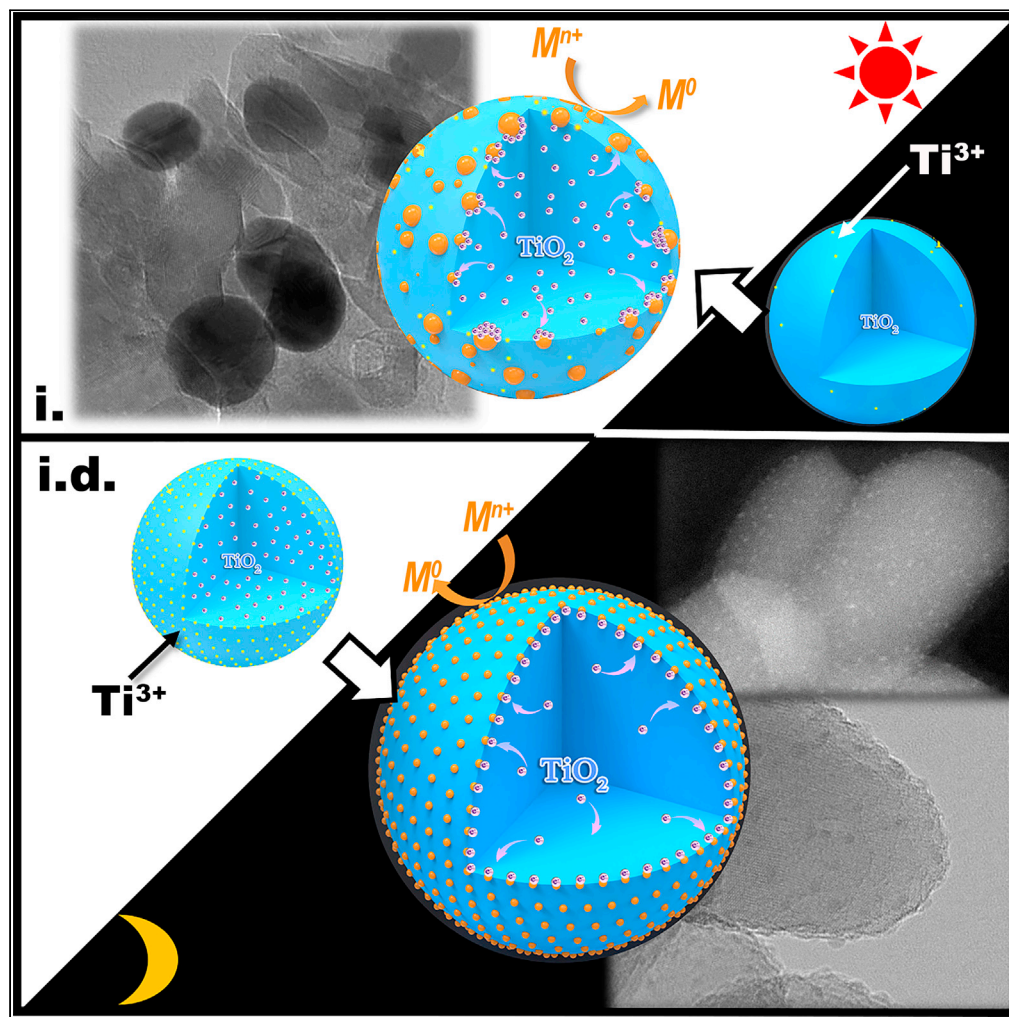# iScience

Article

Photo-assisted sequential assembling of uniform metal nanoclusters on semiconductor support

Haocheng Wu, Wentao Jiang, Liyi Shi, Rengui Li, Lei Huang, Can Li

rgli@dicp.ac.cn (R.L.)
leihuang@shu.edu.cn (L.H.)

Highlights

Metal nanoclusters were deposited on semiconductors via sequential photodeposition

Ti^{3+} species store the photoelectrons and optimize the nucleation and growth processes

The catalysts exhibit superior performance in catalytic oxidation of HCHO

Article

Photo-assisted sequential assembling of uniform metal nanoclusters on semiconductor support

Haocheng Wu,[1] Wentao Jiang,[1] Liyi Shi,[1] Rengui Li,[2,*] Lei Huang,[1,3,*] and Can Li[2]

SUMMARY

Dispersing metal nanoclusters on the oxide supports is attracting close attention in heterogeneous catalysis, but great challenges still lie in controlling the size and dispersion of nanoclusters due to the inevitable agglomeration. Here, we propose a sequential photochemical deposition strategy named "first store, and then release" to uniformly fabricate the size-controlling noble metal nanoclusters on semiconductor oxides. Using the typical semiconductor TiO_2, the photoexcited electrons can be first stored as reduced species (e.g. Ti^{3+}) under irradiation and the Ti^{3+} species can optimize both the nucleation and growth processes in dark reaction, resulting in a uniform dispersing of various noble metals (Au, Pt, Ag etc.) with size diameters of $\sim$1 nm. The nanoclusters catalysts exhibited superior performance in catalytic oxidation of HCHO compared with that of nanoparticles. This work brings a new and useful strategy to construct size-controlling noble metals on the oxide supports for heterogeneous catalysis and the related fields.

INTRODUCTION

Dispersing noble metal nanoparticles and nanoclusters on the oxide supports plays an enormous role in heterogeneous catalysis, which is particularly significant in understanding the size-dependent electronic, structural, and chemical properties of metal clusters catalysts (Heiz and Bullock, 2004; Li et al., 2017; Santra and Goodman, 2003). Many efforts have been devoted to creating uniformly dispersed noble metal catalysts with small nanoparticles even clusters for high efficiency and selectivity owing to their advantages in high surface free energy, low coordination number as well as unique metal-support interactions (Cao et al., 2016). However, great challenges still lie on difficulties in controlling the uniform dispersion of noble metal nanoclusters due to the natural tendency for metal atoms to agglomerate, which usually results in the coexistence of multiple forms including wide size-ranged nanoparticles and clusters (Ji et al., 2017; Liu et al., 2017a). Most of the widely used methods for preparing noble metal nanoclusters usually follow a pre-depositing of precursors using impregnation, hydrothermal, atomic layer deposition, or surfactant protection, and then require a high-temperature (normally higher than 300°C) reduction process to metallic states in reductive atmospheres (e.g. H_2) (Jiang et al., 2015). However, aggregation can be easily triggered under the harsh high-temperature conditions (Cardenas-Lizana et al., 2009). Moreover, organic surfactants are extensively employed to coordinate with metal atoms for maintaining the smaller size of noble metals, which should be removed completely under a relative harsh condition, which also significantly affect the properties of catalysts (Nguyen et al., 2017). Therefore, assembling of uniform noble metal nanoparticles and nanoclusters under mild conditions is urgently demanded in heterogeneous catalysis.

Photochemical deposition process using high-energetic photogenerated charges provides an alternative strategy to realize the deposition of noble metals on the semiconductor oxide supports at room temperature (Clark and Vondjidis, 1965; Kraeutler and Bard, 1978; Oros-Ruiz et al., 2011). Different from normal methods, the semiconductor supports are the sources of photogenerated charges, which participate in the nucleation and growth process of noble metal nanoparticles subsequently (Jiang et al., 2016; Ma et al., 2018). Principally, the photochemical deposition of noble metals is triggered by the photogenerated electrons excited valance bands (VB) to conduction bands (CB) and transferred to the semiconductor surfaces to reduce the noble metal precursors under light irradiation (Zhai et al., 2013; Zhang et al., 2016). Despite of the extensive applications in depositing cocatalysts onto the surface of semiconductors in

[1]Research Center of Nano Science and Technology, College of Sciences, Shanghai University, Shanghai 200444, P. R. China

[2]State Key Laboratory of Catalysis, Dalian National Laboratory for Clean Energy, Dalian Institute of Chemical Physics, Chinese Academy of Sciences, Dalian 116023, P. R. China

[3]Lead contact

*Correspondence: rgli@dicp.ac.cn (R.L.), leihuang@shu.edu.cn (L.H.)

https://doi.org/10.1016/j.isci. 2021.103572

photocatalysis (Li et al., 2020b; Liu et al., 2017), the photochemical deposition of noble metals still possesses challenges in controlling small nanoparticles owing to the preferable accumulation of photogenerated electrons on the noble metals once the initial nucleation takes place, which is originated from the negative Fermi level of noble metals and the formation of Schottky junction (Devi and Kavitha, 2016). In this case, the large accumulation of photogenerated electrons involves in the reduction of noble metals near the nucleation sites, leading to the formation of large nanoparticles and non-uniform distributions (Tanaka et al., 2012). Different strategies including adjusting the adsorption behavior (Liu et al., 2016; Zhang et al., 2004) and surface states of semiconductors (Huang et al., 2020; Zhou et al., 2020) have been developed to control the particle sizes. However, tuning the behaviors of photogenerated charges to participate in the nucleation and growth of noble metals for assembling uniform nanoparticles or nanoclusters is rarely realized.

In this work, taking noble metals (e.g. Au, Ag, Pt, and Pd) loaded titanium oxides (TiO$_2$) as a prototype, an innovative sequential photochemical deposition strategy was put forward following a "first store, and then release" process. We demonstrate that photoinduced generation of Ti^{3+} species on the surface of TiO$_2$ acts as a charges storage sink to store the photogenerated electrons under light conditions; then, the noble metal precursors were introduced to nuclear and consume the photogenerated charges gradually, resulting in the uniform deposition of noble metals nanoclusters with narrow distributions on the TiO$_2$support. The uniformly dispersed M/TiO$_2$ catalysts exhibit remarkably enhanced activities in catalytic oxidation of HCHO compared with the nanoparticles. Such sequential assembling strategy is applicable to various metals and metal oxide supports, which is expected to be promising in fabricating supported catalysts in heterogeneous catalysis.

RESULTS AND DISCUSSION

One of the representative metal oxides, rutile TiO$_2$ (TiO$_2$(R)), was introduced as the support to investigate the noble metals deposited by traditional photodeposition and "first store, and then release" processes. The schematical description for the differences on two deposition processes is shown in Figure S1. The traditional photodeposition process with continuous light irradiation can be denoted as (i.) while the "first store, and then release" process contains a light irradiation and a dark deposition, which is denoted as (i.d.). Figures 1 and S2 present the HRTEM images and the size distributions of various noble metals (Au, Ag, Pt, and Pd) deposited on the TiO$_2$(R) support via two different processes. It clearly shows that the mean particle sizes of the four noble metals are from several nanometers to dozens of nanometers, especially for Au is 13.0 nm and for Ag is 14.0 nm. Moreover, the size distribution of the four metals is quite large and non-uniform, the big particles of Au and Ag are larger than 30 nm. Very differently, the i.d. method shows a remarkable advantage in controlling the size and size distribution. The mean particle sizes of all the four metals are smaller than 1.0 nm. Meanwhile, the size distributions of the nanoparticles well focus in 3.0 nm, even for both Au and Ag. The small particle sizes and size distribution are further confirmed by the HAADF-STEM characterization (Figure S3). This result demonstrates the advantage of developed i.d. method in controlling the size and size distribution of different nobles on TiO$_2$ compared with the traditional i. method.

The loading amounts of different metals on TiO$_2$(R) are further checked by inductively coupled plasma emission spectroscopy (ICP). Table S1 shows that both Au and Pt were completely loaded on TiO$_2$(R) by i. and i.d. methods. Compared with other works (Toledo-Camacho et al., 2021; Al-Madanat et al., 2021; Galeano et al., 2019; Diak et al., 2015; Haselmann et al., 2020), the i.d. method adopted in this paper can realize the deposition of high loading amount and uniform sub-nano noble metal particles on TiO$_2$. With similar loading amount, both Au and Pd showed big difference in the size and size distribution, illustrating that the difference in nucleation and growth process of i. and i.d. methods might play a significant role. The crystalline structure and optical properties of different samples were studied by X-ray diffraction (XRD) (Figure S4) and UV-visible diffuse reflectance spectrum (UV–Vis DRS) (Figure S5). The obvious diffraction peaks and plasmon absorption peak ascribed to Au and Ag further demonstrated the bigger sizes of nanoparticles prepared by i. method. It is worth mentioning that according to the Scherrer equation, Au (i.d)/TiO$_2$ (R) and Au (i.)/TiO$_2$ (R) prepared by 10 mL of HAuCl$_4$ (3.8 mM) have Au particle sizes of 19.1 nm and 16.6 nm, respectively. Fortunately, we demonstrated that proper concentrations (e.g. 0.38 mM for Au) of metal precursors could further optimize the deposition process to avoid the formation of large nanoparticles (Figure S4C). The determination of the oxidation states of the noble metals prepared by i.d. method can be accomplished by the X-ray photoelectron spectroscopy (XPS) study, as shown in Figure S6.The
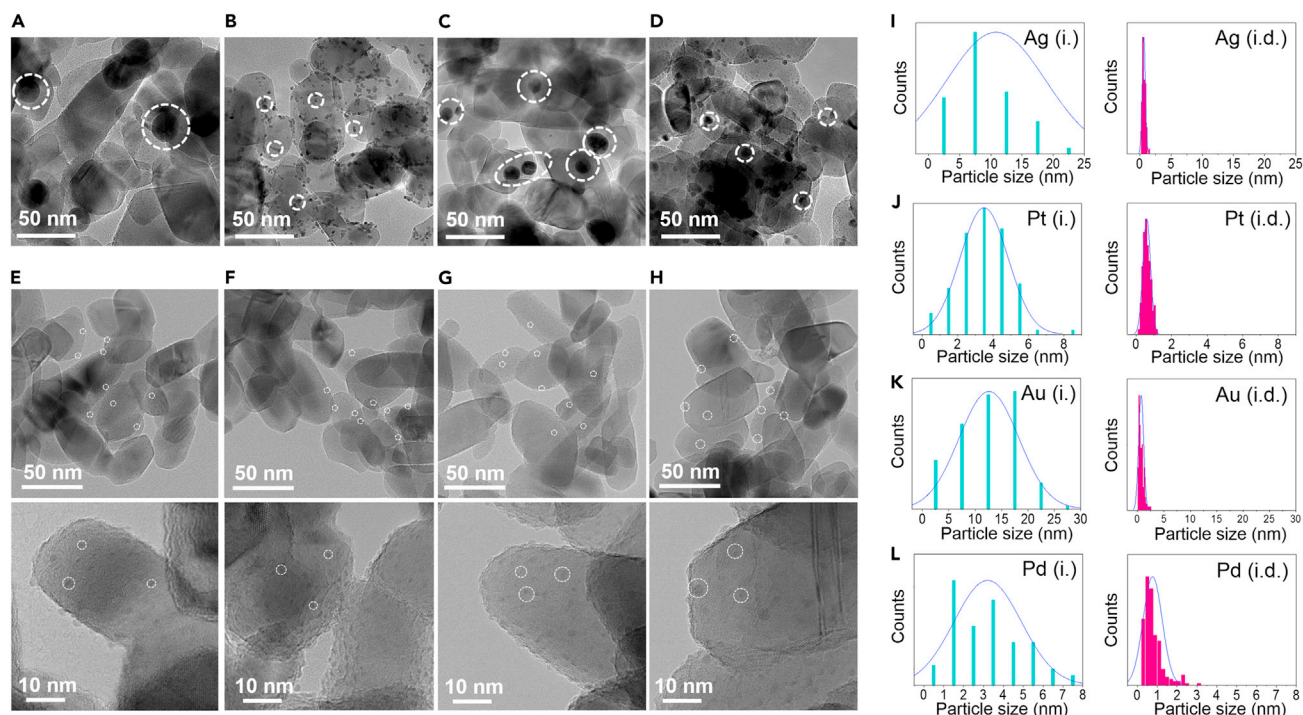
Figure 1. TEM, HRTEM images of different noble metals (Ag, Pt, Au, and Pd) on TiO$_2$(R) by i. and i.d. method and the corresponding particle size distribution

(A–L) (A) Ag (i.)/TiO$_2$(R), (B) Pt (i.)/TiO$_2$(R), (C) Au (i.)/TiO$_2$(R), (D) Pd (i.)/TiO$_2$(R), (E) Ag (i.d.)/TiO$_2$(R), (F) Pt (i.d.)/TiO$_2$(R), (G) Au (i.d.)/TiO$_2$(R), and (H) Pd (i.d.)/TiO$_2$(R). (I–L) are the corresponding particle size distribution of (A–H).

peaks are fitted and corresponding valence states and ratio of different noble metals were summarized in Table S2. The results clearly show that the noble metals in four samples of M (i.d.)/TiO$_2$ are mainly in the natural state and accompanied by a small amount of oxidation state. Figure S7 shows that the ratio of metallic metals could be adjusted by the irradiation duration. The mixed valence states of different metals obtained by i.d. method are similar to the samples prepared by traditional photodeposition process (Hidalgo et al., 2011; Kong et al., 2013; Rodriguez-Gonzalez et al., 2010; Wu et al., 2016).

As the "first store, and then release" deposition process requires the photoexitation of support to provide photogenerated charges, some other metal oxide supports such as anatase TiO$_2$, P25, and ZrO$_2$ were also introduced to investigate the universal of this method. Both Au and Pt were confirmed completely loaded on the above supports (Table S3). As shown in Figures 2 and S8, the mean sizes of both Au and Pt are smaller than 1.0 nm and the size distribution also focuses smaller than 3.0 nm on different oxide supports, which is very identical to the size on TiO$_2$(R). On the opposite, the metals prepared by i. method also have bigger sizes and wide size distributions. The difference in particle sizes is also supported by XRD and UV–Vis DRS spectra (Figures S9 and S10). It is worth mentioning that a peak according to the localized surface plasmon resonance (LSPR) peak of Au is observed for both Au (i.d.)/TiO$_2$ (P25) and Au (i.d.)/TiO$_2$ (A). This might be due to the formation of some Au NPs with bigger size compared with that on TiO$_2$(R). However, the LSPR peak is still quite lower than that of samples prepared by i. method, indicating that i.d. method is still better in controlling the sizes on both TiO$_2$ (P25) and TiO$_2$ (A). Above results further demonstrate the superiority of i.d. method in controlling the size of metals on semiconductors by photodeposition.

It is recognized that the electrostatic adsorption between the supports and the metal precursors is important in the deposition process (Herrmann et al., 1986). The influence of charge properties of different metal precursors on the deposition process then was studied. The zeta potential of TiO$_2$(R) is +11.2 mV. Figure 3A indicates that the negatively charged metal precursors, e.g., AuCl$_4^-$ and PtCl$_6^{2-}$, are prone to load on TiO$_2$(R), while positively charged Ag$^+$ and Pd^{2+} are difficult to load on TiO$_2$(R) (Table S1). Pt was also found difficult to load on TiO$_2$(R) when PtCl$_6^{2-}$ is replaced by positive Pt (NH$_3$)$_4^{2+}$. Above results demonstrate that the opposite charged state of the supporter-precursor combination could achieve high loading without the
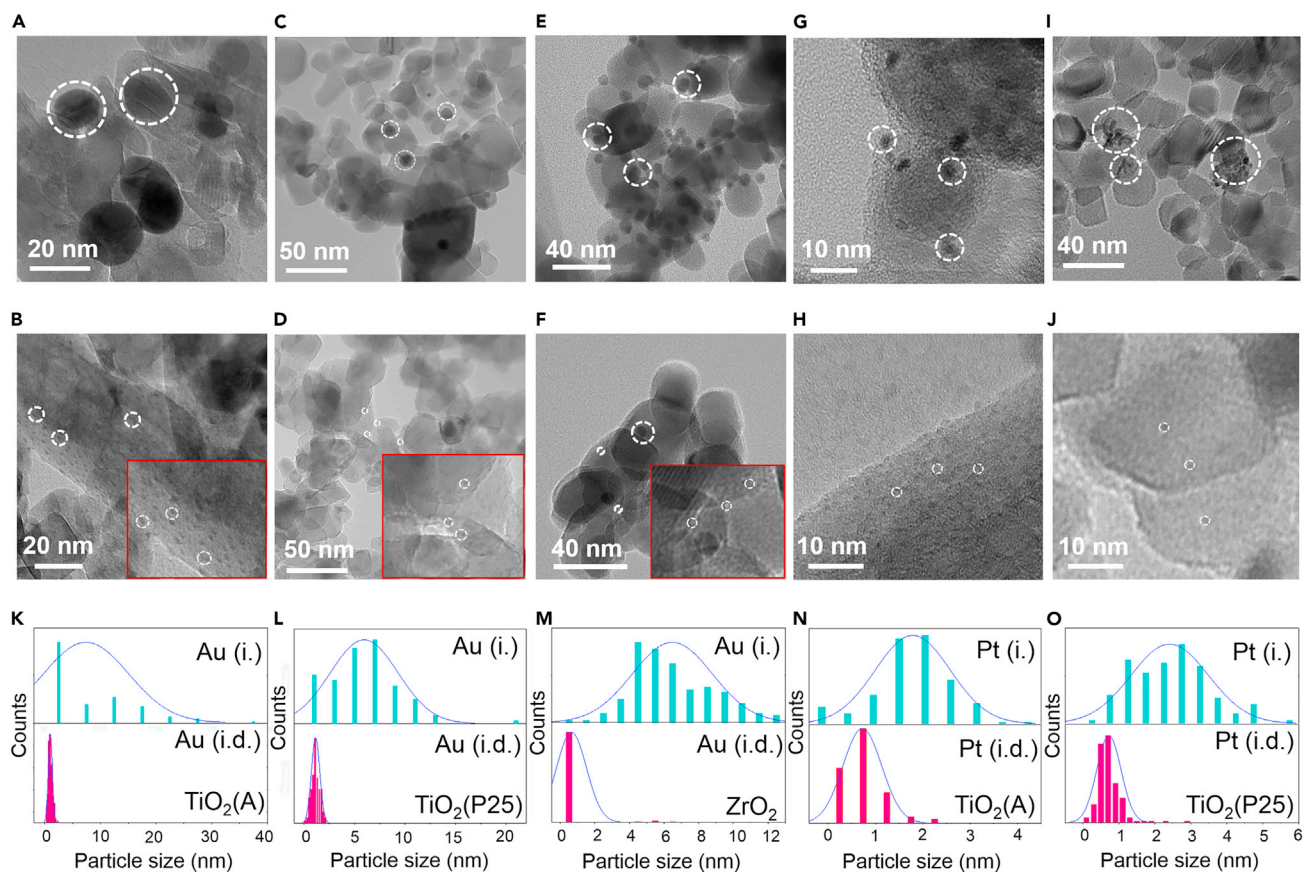
Figure 2. TEM and HRTEM images of Au/Pt supported on other crystal phases of TiO$_2$ and other semiconductors by i. and i.d. methods and the corresponding particle size distribution

(A–O) (A) Au (i.)/TiO$_2$ (A), (B) Au (i.d.)/TiO$_2$ (A), (C) 0.5 wt.% Au (i.)/TiO$_2$ (P25), (D) 0.5 wt.% Au (i.d.)/TiO$_2$ (P25), (E) Au (i.)/ZrO$_2$, (F) Au (i.d.)/ZrO$_2$, (G) Pt (i.)/TiO$_2$ (A), (H) Pt (i.d.)/TiO$_2$ (A), (I) 0.5 wt.% Pt (i.)/TiO$_2$ (P25), and (J) 0.5 wt.% Pt (i.d.)/TiO$_2$ (P25). (K–O) are the corresponding particle size distribution.

waste of metal precursors, while the same changes prone to cause the incomplete loading. Therefore, i.d. method is suitable for the combination of noble metal precursors and supports with strong electrostatic adsorption.

Many studies have proved that the nucleation and growth processes are key factors affecting the particle size and distribution, and are closely related to the kinetics of chemical reactions (Liu et al., 2014; Viau et al., 2001). In the photodeposition process, when noble metals nucleate on semiconductors, a Schottky junction forms and increases the separation of photogenerated electrons and holes. The transfer of photogenerated electrons to the loaded metals leads to a rapid and uneven growth of metal particles, and therefore the uncontrollable particle sizes. Figure 3B shows that the photodeposition of Pt is very fast as indicated by the fully consumption of $PtCl_6^{2-}$ in only 5 min. Differently, the i.d. method showed much slower deposition process which takes about 30 min and the whole process is well controlled. The well-controlled deposition rate might be one of the important factors to effectively control the particle size.

Following the above hypothesis, using other way to decrease the rate of nucleation and growth might also achieve similar results of i.d. method. We then decreased the irradiation intensity from 74.0 to 2.3 mW/cm^2 to reduce the amounts of photoelectrons and then decrease the rate of photodeposition process. Figure S11A shows that the mean size of Au is about 10.8 nm while the size distribution is in the range of 0.5∼35 nm over Au (i.)/TiO$_2$. Similar trend is also supported by the UV–Vis DRS spectra that the absorption peak of Au (i.)/TiO$_2$ almost keeps the same under different irradiation condition, as Figure S12. The unchanged absorption peak of Au reflects the similar size and size distribution. Combined with the results
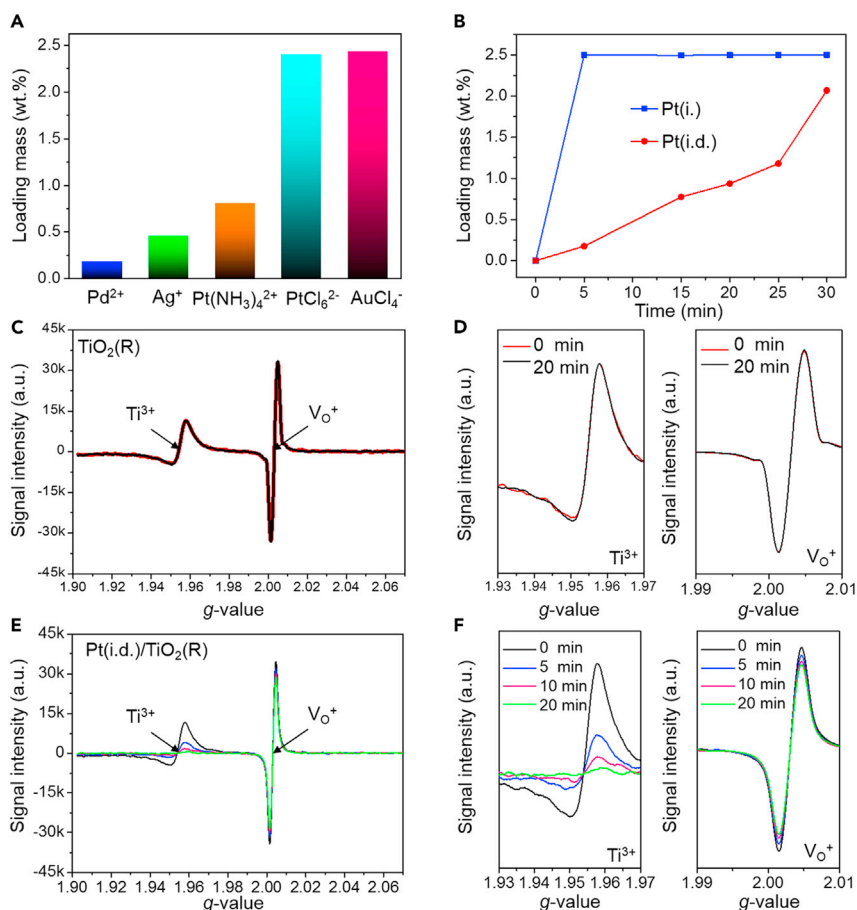
Figure 3. Photodeposition process characterization

(A) Comparison of loading capacities of noble metal precursors with different charges using the i.d. method.

(B) Comparison of deposition rates of Pt by i. and i.d. methods. *In situ* EPR spectra collected under dark reaction in i.d. method upon.

(C and E) (C) Pure TiO_2(R) and (E) Pt/TiO_2.

(D and F) are local spectra of (C) and (E), correspondingly.

above, it is deduced that there might be some other factors for size control beyond the controlled deposition rate of noble metals.

It has repeatedly verified that the surface property is also significant in the nucleation and growth process.[14] In this work, the semiconductors are irradiated and the surface properties might change during this process for the i.d. method. To further identify the influences of irradiated surfaces on the deposition process, we designed an i.i. method, namely irradiate the semiconductors first and then add the metal precursors for the following photodeposition. Compared with the i. method, the surface was modified by the irradiation before the photodeposition process. Interestingly, the mean size of Au nanoparticles obviously decreased (4.5 nm) compared with that of Au (i.)/TiO_2 (12.4 nm), as Figure S11B. The accompanying increased number of Au nanoparticles indicates that the irradiation modified surface is beneficial to increase the sites for nucleation. On the other hand, the size of Au NPs is also much bigger and uneven compared with that of Au (i.d.)/TiO_2 (0.2~2.3 nm, 0.7 nm), which further proves that the deposition rate is also important. It is therefore concluded that both the controlled deposition rate and the irradiation modified surface played significant roles in the fabrication of metal nanoclusters on semiconductor supports.

It is well known that electron-hole pairs are created in TiO_2 when exposed to ultra-bandgap illumination (Al-Madanat et al., 2021; Eagles, 1964) and the conduction band electrons can be trapped on the Ti^{4+} ions to form the Ti^{3+} species (Lan et al., 2020), which make the color of TiO_2 blue (Torimoto et al., 1996). In the i.d. process, we did
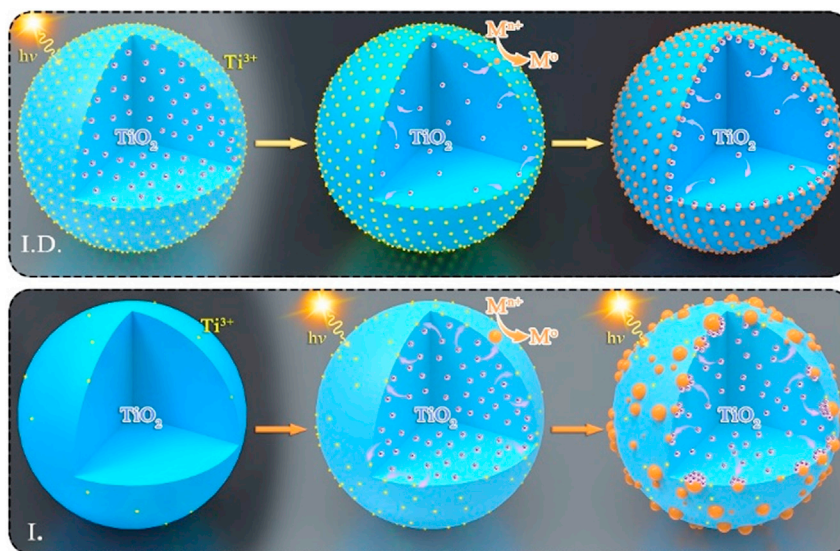
Figure 4. Schematic diagram of the mechanism for particle size and distribution control of i. method and i.d. method

find that the TiO_2 suspension changed blue after 30 min of irradiation as shown in Figure S13A. Besides, it is observed that the XPS peak according to Ti 2p3/2 shifted to lower binding energy after irradiation (Figure S13B). These results indicate that Ti^{3+} species formed in TiO_2 with the irradiation. The evolution of the photoinduced Ti^{3+} in the presence and absence of H_2PtCl_6 were studied by *in situ* electron paramagnetic resonance (EPR) measurements as shown in Figures 3C–3F. Two signals with g = 2.004 assigned to the characteristic of single-electron-trapped oxygen vacancies and g = 1.954 attributed to the lattice electron trapping sites (Ti^{3+}) in the bulk of TiO_2 are observed in both cases (Liu et al., 2015), confirming that Ti^{3+} species were generated in the "i." step. Without irradiation and H_2PtCl_6, no signals according to Ti^{3+} and oxygen vacancies were observed (Figure S13C). Without H_2PtCl_6, no significant attenuation of signal intensity was observed within 20 min in the dark (Figures 3C and 3D), indicating that the Ti^{3+} species could maintain for a while in the dark. However, when H_2PtCl_6 precursor was added, the signal intensity of Ti^{3+} decreased significantly with time (Figures 3E and 3F), illustrating that the Ti^{3+} could be consumed by H_2PtCl_6, which driven the deposition of Pt on TiO_2. According to previous study (Wenderich and Mul, 2016; Zhao et al., 2019), the potential of Ti^{4+}/Ti^{3+} species located about 0.8 to 1.3 eV lower than the conduction band (CB) of TiO_2, and can thermodynamically reduce different metal precursors such as $AgNO_3$, H_2PtCl_6, $HAuCl_4$, and $PdCl_2$ (Figure S14). In order to exclude the influence of residual methanol and other organics in the deposition of metal clusters, we removed the residual methanol and other organics after the TiO_2 suspension was irradiated through a rapid separation and washing process, then quickly redispersed the solid TiO_2 into DI water and added metal precursor solution for the deposition under dark conditions. The corresponding TEM image (Figure S15) shows that Au clusters could be obtained without methanol or other organics. Besides, the photolysis of the metal precursors is also ruled out for the formation of metal clusters because the deposition conducts in the dark rather than in the irradiation. Above results confirm that Ti^{3+} species are the main sites for reducing precursors and the main reason for the increase of nucleation sites.

Based on the above results and discussion, we propose a possible mechanism to address the size control of the developed i.d. method as shown in Figure 4. In the irradiation stage, the photocatalytic semiconductors are excited and the charges are separated. The photogenerated holes are quickly consumed owing to the presence of methanol, and the accumulated photogenerated electrons can reduce TiO_2 to form Ti^{3+}. In the dark reaction stage, these stored Ti^{3+} can be used to reduce the introduced noble metal precursors, driving the nucleation and growth of noble metals on semiconductors. In this process, Ti^{3+} not only increases the nucleation sites but also effectively controls the growth rate because its reduction ability is weaker than the photoelectrons in CB. Increased nucleation sites and controlled growth rate make the formation of metal nanoclusters on oxides. As for i. method, photoelectrons in CB are the main species for the reduction of metal precursors. The higher reducibility and the Schottky junction induced rapid accumulation of photoelectrons make the nuclear and growth rate uncontrollable. Large and wide size dispersion of metal nanoparticles is achieved.
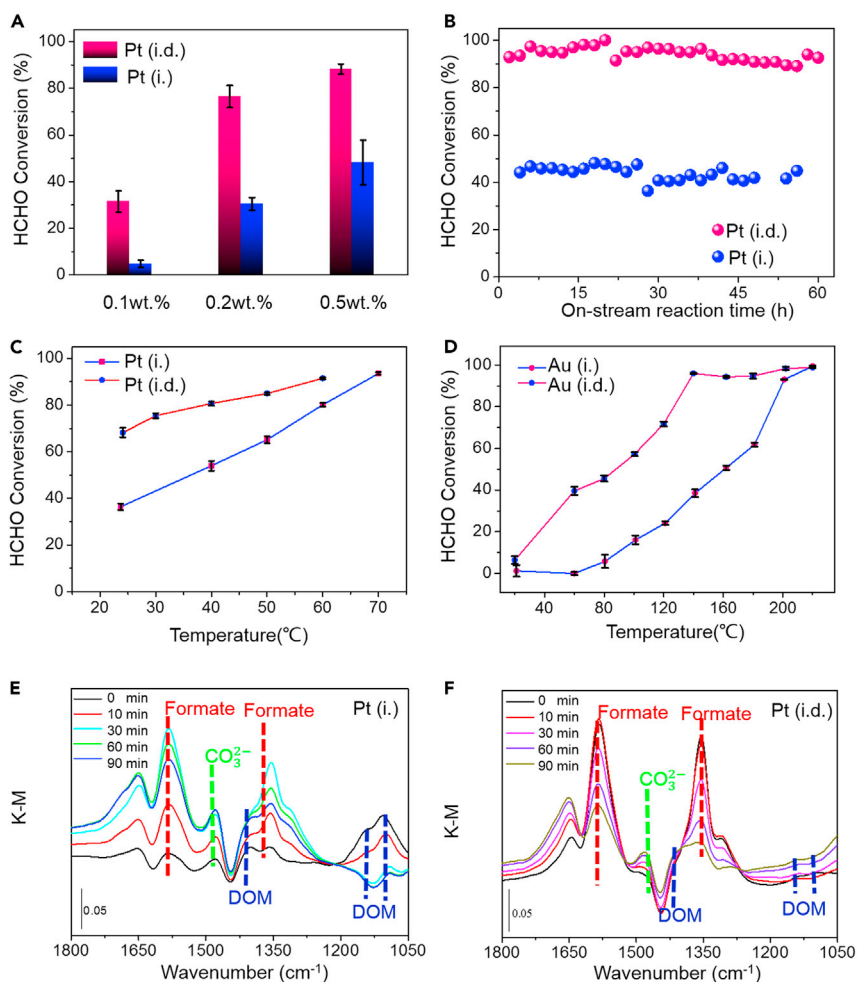
Figure 5. HCHO catalytic oxidation performance

(A) HCHO conversion over x wt.% Pt/TiO$_2$ (P25) (x = 0.1, 0.2, 0.5) catalysts synthesized by i. and i.d. methods at 25°C. The error bar data obtained based on 5 times of tests.

(B) Stability test of 0.5 wt.% Pt(i.d.)/TiO$_2$ (P25) and 0.5 wt.% Pt(i.)/TiO$_2$ (P25).

(C) HCHO conversion over 0.5 wt.% Pt/TiO$_2$ (P25) catalysts synthesized by i. and i.d. methods as a function temperature. The error bar data obtained based on 3 times of tests.

(D) HCHO conversion over 0.5 wt.% Au/TiO$_2$ (P25) catalysts synthesized by i. and i.d. methods as a function temperature. Above reaction conditions: HCHO δ = 200 ppm, O$_2$ 20 vol%, N$_2$ balance, total flow rate of 250 mL min^{-1}, and GHSV 35000 h^{-1}. The error bar data obtained based on 3 times of tests.

(E and F) (E) and (F) are the In-situ DRIFTS local spectra over 0.5 wt.% Pt(i.)/TiO$_2$ (P25) and 0.5 wt.% Pt(i.d.)/TiO$_2$ (P25) after a flow of HCHO + Ar for 30 min followed by Ar purging for 10 min and finally O$_2$ purging for 90 min at 25°C, respectively. The full spectra are in Figure S13. HCHO δ = 50 ppm, O$_2$ 20 vol%, N$_2$ balance, and total flow rate of 50 mL min^{-1}.

As demonstrated above, uniformly distributed noble metal nanoclusters and nanoparticles can be precisely controlled via a "first store, and then release" deposition process, which provides the possibility to fabricate the well-designed supported catalysts. In our experiment, typical catalytic oxidation of formaldehyde (HCHO) was evaluated as a model reaction in which the noble-metal supported catalysts are widely used (Duan et al., 2019; Zhang et al., 2012). Figure 5A shows that the activities of Pt (i.d.)/TiO$_2$ (P25) with different Pt loading amounts are much higher than that of the samples of Pt (i.)/TiO$_2$ (P25) at room temperature. Within an on-stream reaction time of 60 h, the conversion of HCHO remains unchanged at room temperature for both samples (Figure 5B). As for Au/TiO$_2$ (P25), the T90% of Au(i.d.)/TiO$_2$ (P25) and Au(i.)/TiO$_2$ (P25) are 135°C and 200°C, respectively (Figure 5C), demonstrating that the Au nanoclusters prepared by i.d. method have much better performance compared with that of by i. method over TiO$_2$. It is worth mentioning that Pt/TiO$_2$ (P25) and Au/TiO$_2$ (P25) prepared by i.d. method have better

performance in the catalytic oxidation of formaldehyde compared with recently reported works (Li et al., 2020a; Shi et al., 2019; Eom et al., 2020; Zhang et al., 2006), as shown in Table S4. The mechanism of catalytic conversion of HCHO onto Pt(i.)/TiO$_2$ and Pt(i.d.)/TiO$_2$ was investigated in detail by *in situ* infrared diffuse reflectance (FTIR) spectroscopy. As illustrated in Figures 5E and 5F and Figure S16, the characteristic absorption peaks of various intermediates, formate species (HCOO*), dioxomethyl (DOM), and carbonate (CO$_3^{2-}$) evidently appear during the reaction process (Table S5).

Interestingly, absorbed HCHO is mainly in the form of DOM on Pt(i.)/TiO$_2$ (P25) while in the form of formate species on Pt(i.d.)/TiO$_2$ (P25) before exposed to O$_2$. According to previous study, HCHO is firstly adsorbed on TiO$_2$ in the form of DOM and then oxidized to formate species (e.g. HCOO*) in a normal case (He et al., 2019; Kwon et al., 2015; Rui et al., 2014). Here, formate species already formed on Pt(i.d.)/TiO$_2$ (P25) without the introduction of O$_2$, indicating that DOM is oxidized by the active oxygen species attributed to the formed Pt nanoclusters. This conclusion is also supported by the H$_2$-TPR results (Figure S17) (Kim et al., 2012). When O$_2$ is introduced, the amount of formate species increased first and then decreased (after 10 min) on Pt(i.d.)/TiO$_2$ (P25) (Figure S18). The signal according to carbonate species increased meanwhile. As for Pt(i.)/TiO$_2$ (P25), the amount of DOM decreased quickly and the formate species also experienced an increase and decrease (after 30 min) process and the carbonate species also formed in this case. The results indicate that the oxidation of HCHO follows a process of HCHO → DOM → formate species → carbonate species on both Pt(i.)/TiO$_2$ (P25) and Pt(i.d.)/TiO$_2$ (P25). However, the oxidation of DOM to formate species is much favorable on Pt(i.d.)/TiO$_2$ (P25), which is possibly due to the stronger and more active oxygen species benefited by the uniform Pt nanoclusters dispersed on the TiO$_2$support.

Conclusions

In conclusion, we developed a universal and convenient strategy to load uniform metal nanoclusters on oxides. The strategy has demonstrated effective on different metals, supports, and crystal phases. The proposed "first store, and then release" process can store a large number of reduced species (e.g. Ti^{3+}) and therefore effectively optimize both the nuclear and growth process. The obtained Pt nanoclusters have obvious promoted catalytic performance in the catalytic oxidation of HCHO compared with that of nanoparticles, which is attributed to the formation of more and active oxygen species. This research not only brings new ideas in fabrication of uniform metal nanoclusters on oxides but also in understanding the nucleation and growth of metals in photodeposition process.

Limitations of the study

Noting that such a photo-assisted sequential assembling methodology requires the semiconductor support enables to store photogenerated charges via a redox process, so not all the semiconductor supports are applicable.

STAR★METHODS

Detailed methods are provided in the online version of this paper and include the following:

- KEY RESOURCES TABLE
- RESOURCE AVAILABILITY
  - Lead contact
  - Materials availability
  - Data and code availability
- METHOD DETAILS
  - Preparation of samples
  - Catalytic performance test
  - Methods for characterization

AUTHOR CONTRIBUTIONS

DECLARATION OF INTERESTS

REFERENCES

Al-Madanat, O., AlSalka, Y., Dillert, R., and Bahnemann, D.W. (2021). Photocatalytic H_2 production from naphthalene by various TiO_2 photocatalysts: Impact of Pt loading and formation of intermediates. Catalysts 11, 20.

Cao, S.W., Tao, F., Tang, Y., Li, Y.T., and Yu, J.G. (2016). Size-and shape-dependent catalytic performances of oxidation and reduction reactions on nanocatalysts. Chem. Soc. Rev. 45, 4747–4765.

Cardenas-Lizana, F., Gomez-Quero, S., Idriss, H., and Keane, M.A. (2009). Gold particle size effects in the gas-phase hydrogenation of m-dinitrobenzene over Au/TiO_2. J. Catal. 268, 223–234.

Clark, W.C., and Vondjidis, A.G. (1965). An infrared study of the photocatalytic reaction between titanium dioxide and silver nitrate. J. Catal. 4, 691–696.

Devi, L.G., and Kavitha, R. (2016). A review on plasmonic metal-TiO_2 composite for generation, trapping, storing and dynamic vectorial transfer of photogenerated electrons across the Schottky junction in a photocatalytic system. Appl. Surf. Sci. 360, 601–622.

Diak, M., Grabowska, E., and Zaleska, A. (2015). Synthesis, characterization and photocatalytic activity of noble metal-modified TiO_2 nanosheets with exposed {001} facets. Appl. Surf. Sci. 347, 275–285.

Duan, L.J., Liu, H., Muhammad, Y., Shi, L.Y., Wu, H.C., Zhang, J.P., Yu, D.Q., and Huang, L. (2019). Photo-mediated co-loading of highly dispersed MnO_x-Pt on g-C_3N_4 boosts the ambient catalytic oxidation of formaldehyde. Nanoscale 11, 8160–8169.

Eagles, D.M. (1964). Polar modes of lattice vibration and polaron coupling constants in rutile (TiO_2). J. Phy. Chem. Sol. 25, 1243–1251.

Eom, H., Hwang, I.H., Lee, D.Y., Lee, S.M., and Kim, S.S. (2020). Preparation of liquid-phase reduction method-based Pt/TiO_2 catalyst and reaction characteristics during HCHO room-temperature oxidation. Ind. Eng. Chem. Res. 59, 15489–15496.

Galeano, L., Valencia, S., Marin, J.M., Restrepo, G., Navio, J.A., and Hidalgo, M.C. (2019). Comparison of the effects generated by the dry-soft grinding and the photodeposition of Au and Pt processes on the visible light absorption and photoactivity of TiO_2. Mater. Res. Express 6, 1050d9.

Haselmann, G.M., Baumgartner, B., Wang, J., Wieland, K., Gupta, T., Herzig, C., Limbeck, A., Lendl, B., and Eder, D. (2020). In situ Pt photodeposition and methanol photooxidation on Pt/TiO_2: Pt-loading-dependent photocatalytic reaction pathways studied by liquid-phase infrared spectroscopy. ACS Catal. 10, 2964–2977.

He, M., Ji, J., Liu, B.Y., and Huang, H.B. (2019). Reduced TiO_2 with tunable oxygen vacancies for catalytic oxidation of formaldehyde at room temperature. Appl. Surf. Sci. 473, 934–942.

Heiz, U., and Bullock, E.L. (2004). Fundamental aspects of catalysis on supported metal clusters. J. Mater. Chem. 14, 564–577.

Herrmann, J.M., Disdier, J., and Pichat, P. (1986). Photoassisted platinum deposition on TiO_2 powder using various platinum complexes. J. Phys. Chem. 90, 6028–6034.

Hidalgo, M.C., Murcia, J.J., Navio, J.A., and Colon, G. (2011). Photodeposition of gold on titanium dioxide for photocatalytic phenol oxidation. Appl. Catal. A: Gen. 397, 112–120.

Huang, L., Liu, X., Wu, H., Wang, X., Wu, H., Li, R., Shi, L., and Li, C. (2020). Surface state modulation for size-controllable photodeposition of noble metal nanoparticles on semiconductors. J. Mater. Chem. A 8, 21094–21102.

Ji, S.F., Chen, Y.J., Fu, Q., Chen, Y.F., Dong, J.C., Chen, W.X., Li, Z., Wang, Y., Gu, L., He, W., et al. (2017). Confined pyrolysis within metal-organic frameworks to form uniform Ru_3 clusters for efficient oxidation of alcohols. J. Am. Chem. Soc. 139, 9795–9798.

Jiang, X.L., Fu, X.L., Zhang, L., Meng, S.G., and Chen, S.F. (2015). Photocatalytic reforming of glycerol for H_2 evolution on Pt/TiO_2: Fundamental understanding the effect of co-

catalyst Pt and the Pt deposition route. J. Mater. Chem. A 3, 2271–2282.

Jiang, Z., Zhang, Z.Y., Shangguan, W.F., Isaacs, M.A., Durndell, L.J., Parlett, C.M.A., and Lee, A.F. (2016). Photodeposition as a facile route to tunable Pt photocatalysts for hydrogen production: On the role of methanol. Catal. Sci. Technol. 6, 81–88.

Kim, S.S., Lee, H.H., and Hong, S.C. (2012). The effect of the morphological characteristics of TiO_2 supports on the reverse water-gas shift reaction over Pt/TiO_2 catalysts. Appl. Catal. B: Environ. 119, 100–108.

Kong, W.Z., Tian, B.Z., Zhang, J.L., He, D.N., and Anpo, M. (2013). Microstructure and hydrogen production activity of $Pt-TiO_2$ prepared by precipitation-photodeposition. Res. Chem. Intermed. 39, 1701–1710.

Kraeutler, B., and Bard, A.J. (1978). Heterogeneous photocatalytic preparation of supported catalysts photodeposition of platinum on titanium dioxide powder and other substrates. J. Am. Chem. Soc. 100, 4317–4318.

Kwon, D.W., Seo, P.W., Kim, G.J., and Hong, S.C. (2015). Characteristics of the HCHO oxidation reaction over Pt/TiO_2 catalysts at room temperature: The effect of relative humidity on catalytic activity. Appl. Catal. B: Environ. 163, 436–443.

Lan, K., Wang, R., Wei, Q., Wang, Y., Hong, A., Feng, P., and Zhao, D. (2020). Stable Ti^{3+} defects in oriented mesoporous titania frameworks for efficient photocatalysis. Angew. Chem. Int. Ed. 59, 17676–17683.

Li, L.C., Li, L., Wang, L., Zhao, X.J., Hua, Z.L., Chen, Y.Y., Li, X.B., and Gu, X.L. (2020a). Enhanced catalytic decomposition of formaldehyde in low temperature and dry environment over silicate-decorated titania supported sodium-stabilized platinum catalyst. Appl. Catal. B Environ. 277, 119216.

Li, L., Wang, Y.C., Vanka, S., Mu, X.Y., Mi, Z.T., and Li, C.J. (2017). Nitrogen photofixation over III-nitride nanowires assisted by ruthenium clusters

of low atomicity. Angew. Chem. Int. Ed. 56, 8701–8705.

Li, Z., Zhang, L., Liu, Y., Shao, C.Y., Gao, Y.Y., Fan, F.T., Wang, J.X., Li, J.M., Yan, J.C., Li, R.G., et al. (2020b). Surface polarity-induced spatial charge separation boosts photocatalytic overall water splitting on GaN nanorod Arrays. Angew. Chem. Int. Ed. 59, 935–942.

Liu, J., Wang, W., Shen, T., Zhao, Z., Feng, H., and Cui, F. (2014). One-step synthesis of noble metal/oxide nanocomposites with tunable size of noble metal particles and their size-dependent catalytic activity. RSC Adv. 4, 30624–30629.

Liu, L.C., Diaz, U., Arenal, R., Agostini, G., Concepcion, P., and Corma, A. (2017a). Generation of subnanometric platinum with high stability during transformation of a 2D zeolite into 3D. Nat. Mater. 16, 132–138.

Liu, P.X., Zhao, Y., Qin, R.X., Mo, S.G., Chen, G.X., Gu, L., Chevrier, D.M., Zhang, P., Guo, Q., Zang, D.D., et al. (2016). Photochemical route for synthesizing atomically dispersed palladium catalysts. Science 352, 797–801.

Liu, X.Q., Iocozzia, J., Wang, Y., Cui, X., Chen, Y.H., Zhao, S.Q., Li, Z., and Lin, Z.Q. (2017). Noble metal-metal oxide nanohybrids with tailored nanostructures for efficient solar energy conversion, photocatalysis and environmental remediation. Energy Environ. Sci. 10, 402–434.

Liu, Y., Zhang, B., Luo, L., Chen, X., Wang, Z., Wu, E., Su, D., and Huang, W. (2015). TiO_2/Cu_2O core/ultrathin shell nanorods as efficient and stable photocatalysts for water reduction. Angew. Chem. Int. Ed. 54, 15260–15265.

Ma, J.Q., Guo, X.H., Ge, H.G., Tian, G.H., and Zhang, Q. (2018). Seed-mediated photodeposition route to Ag-decorated SiO_2@TiO_2 microspheres with ideal core-shell structure and enhanced photocatalytic activity. Appl. Surf. Sci. 434, 1007–1014.

Nguyen, T.T., Pham, H.T., and Dao, K.A. (2017). The effects of polyvinylpyrrolidone and thermal annealing on red shifts for absorption spectra of the nanoparticle Au/TiO_2 thin film with different Au ratios. J. Mater. Sci. Mater. Electron. 28, 2075–2085.

Oros-Ruiz, S., Pedraza-Avella, J.A., Guzman, C., Quintana, M., Moctezuma, E., del Angel, G., Gomez, R., and Perez, E. (2011). Effect of gold particle size and deposition method on the photodegradation of 4-chlorophenol by Au/TiO_2. Top. Catal. 54, 519–526.

Rodriguez-Gonzalez, V., Alfaro, S.O., Torres-Martinez, L.M., Cho, S.H., and Lee, S.W. (2010). Silver-TiO_2 nanocomposites: Synthesis and harmful algae bloom UV-photoelimination. Appl. Catal. B: Environ. 98, 229–234.

Rui, Z.B., Chen, L.Y., Chen, H.Y., and Ji, H.B. (2014). Strong metal-support interaction in Pt/TiO_2 induced by mild HCHO and $NaBH_4$ solution reduction and its effect on catalytic toluene combustion. Ind. Eng. Chem. Res. 53, 15879–15888.

Santra, A.K., and Goodman, D.W. (2003). Oxide-supported metal clusters: Models for heterogeneous catalysts. J. Phys. Condes. Matter. 15, R31–R62.

Shi, K.Z., Wang, L., Li, L., Zhao, X.J., Chen, Y.Y., Hua, Z.L., Li, X.B., Gu, X.L., and Li, L.C. (2019). Mild preoxidation treatment of Pt/TiO_2 catalyst and its enhanced low temperature formaldehyde decomposition. Catalysts 9, 694.

Tanaka, A., Ogino, A., Iwaki, M., Hashimoto, K., Ohnuma, A., Amano, F., Ohtani, B., and Kominami, H. (2012). Gold-titanium(IV) oxide plasmonic photocatalysts prepared by a colloid-photodeposition method: Correlation between physical properties and photocatalytic activities. Langmuir 28, 13105–13111.

Toledo-Camacho, S.Y., Rey, A., Maldonado, M.I., Llorca, J., Contreras, S., and Medina, F. (2021). Photocatalytic hydrogen production from water-methanol and -glycerol mixtures using Pd/TiO_2 (-WO_3) catalysts and validation in a solar pilot plant. Int. J. Hydrog. Energy 46, 36152–36166.

Torimoto, T., Fox, R.J., and Fox, M.A. (1996). Photoelectrochemical doping of TiO_2 particles and the effect of charge carrier density on the photocatalytic activity of microporous semiconductor electrode films. J. Electrochem. Soc. 143, 3712–3717.

Viau, G., Toneguzzo, P., Pierrard, A., Acher, O., Fievet-Vincent, F., and Fievet, F. (2001). Heterogeneous nucleation and growth of metal nanoparticles in polyols. Scr. Mater. 44, 2263–2267.

Wenderich, K., and Mul, G. (2016). Methods, mechanism, and applications of photodeposition in photocatalysis: A review. Chem. Rev. 116, 14587–14619.

Wu, M., Zheng, M.J., Han, Y.X., Xu, Z.Y., and Zheng, S.R. (2016). Liquid phase catalytic hydrodebromination of tetrabromobisphenol A on supported Pd catalysts. Appl. Surf. Sci. 376, 113–120.

Zhai, Q.G., Xie, S.J., Fan, W.Q., Zhang, Q.H., Wang, Y., Deng, W.P., and Wang, Y. (2013). Photocatalytic conversion of carbon dioxide with water into methane: Platinum and copper(I) oxide co-catalysts with a core-shell structure. Angew. Chem. Int. Ed. 52, 5776–5779.

Zhang, C.B., He, H., and Tanaka, K. (2006). Catalytic performance and mechanism of a Pt/TiO_2 catalyst for the oxidation of formaldehyde at room temperature. Appl. Catal. B: Environ. 65, 37–43.

Zhang, C.B., Liu, F.D., Zhai, Y.P., Ariga, H., Yi, N., Liu, Y.C., Asakura, K., Flytzani-Stephanopoulos, M., and He, H. (2012). Alkali-metal-promoted Pt/TiO_2 opens a more efficient pathway to formaldehyde oxidation at ambient temperatures. Angew. Chem. Int. Ed. 51, 9628–9632.

Zhang, F.X., Chen, J.X., Zhang, X., Gao, W.L., Jin, R.C., Guan, N.J., and Li, Y.Z. (2004). Synthesis of titania-supported platinum catalyst: The effect of pH on morphology control and valence state during photodeposition. Langmuir 20, 9329–9334.

Zhang, G.G., Lan, Z.A., Lin, L.H., Lin, S., and Wang, X.C. (2016). Overall water splitting by Pt/g-C_3N_4 photocatalysts without using sacrificial agents. Chem. Sci. 7, 3062–3066.

Zhao, Z.Q., Goncalves, R.V., Barman, S.K., Willard, E.J., Byle, E., Perry, R., Wu, Z.K., Huda, M.N., Moule, A.J., and Osterloh, F.E. (2019). Electronic structure basis for enhanced overall water splitting photocatalysis with aluminum doped $SrTiO_3$ in natural sunlight. Energy Environ. Sci. 12, 1385–1395.

Zhou, X., Qian, K., Zhang, Y., Li, D., Wei, Z., Wang, H., Ye, R., Liu, J., Ye, B., and Huang, W. (2020). Tuning the size of photo-deposited metal nanoparticles via manipulating surface defect structures of TiO_2 nanocrystals. Chem. Commun. 56, 1964–1967.

STAR★METHODS

KEY RESOURCES TABLE

REAGENT or RESOURCE	SOURCE	IDENTIFIER
Chemicals, peptides, and recombinant proteins		
Zirconium dioxide	Macklin	CAS: 1314-23-4
Rutile titanium dioxide	Aldrich	CAS: 1317-80-2
Anatase titanium dioxide	Aldrich	CAS: 1317-70-0
Tetraammineplatinum (II) hydroxide hydrate	Aldrich	CAS: 15651-37-3
Chloroplatinic acid hexahydrate	Sinopharm	CAS: 18497-13-7
Chlorauric acid tetrahydrate	Sinopharm	CAS: 16903-35-8
Palladium chloride	Sinopharm	CAS: 7647-10-1
Silver nitrate	Sinopharm	CAS: 7761-88-8
Methanol	Sinopharm	CAS: 67-56-1
Hydrochloric acid	Sinopharm	CAS: 7647-01-0
P25 titanium dioxide	JiangHuTaiBai	CAS: 13463-67-7
Software and algorithms		
Origin 8.5	OriginLab	https://www.originlab.com/
MDI Jade 6	Materials Data Inc.	https://materialsdata.com/
other		
XPS peak 41	TttchehAuto	https://www.tttech-auto.com/

RESOURCE AVAILABILITY

Lead contact

Further information and requests for resources and reagents should be directed to and will be fulfilled by the lead contact, Lei Huang (leihuang@shu.edu.cn).

Materials availability

This study did not generate new unique reagents.

Data and code availability

All data reported in this paper will be shared by the lead contact upon request.

This paper dose not report original code.

Any additional information required to analyze the data reported in this paper is available from the lead contact upon request.

METHOD DETAILS

Preparation of samples

All commercially available reagents were reagent grade and used without further purification.

Preparation of M(i.)/TiO$_2$ is shown in Figure S1A. In general, 0.3 g TiO$_2$ powder was dispersed into 720 mL of deionized water for 30 min by ultrasound (360 W). Subsequently, 100 mL of anhydrous methanol and 10 mL of noble metal precursor solutions (HAuCl$_4$·4H$_2$O, 3.8 mM; H$_2$PtCl$_6$·6H$_2$O, 3.8 mM; Pt(NH$_3$)$_4$(OH)$_2$·× H$_2$O, 3.8 mM; AgNO$_3$, 6.9 mM and PdCl$_2$ 7.0 mM) were added and stirred for 10 min in the dark. After the reaction solution was transferred to the photoreactor (Yuming, YM-GHX-II), N$_2$ (0.4 MPa, 40 mL/min) was injected and sealed the reactor to eliminate the influence of oxygen. Keep stirring, turn on the 500 W side-lit Hg lamp (74 mW/cm^2) to start irradiation reaction (i.). The reaction temperature kept at 13°C $\pm$ 2°C by

circulating water during the whole process. Finally, turn off the lamp after 30 min of irradiation. The precipitation then was collected by extraction and dried at 60°C for 8 h in air atmosphere. Finally, the final sample powder was obtained after grinding.

Preparation of M(i.d.)/TiO$_2$ is shown in Figure S1B. In general, 0.3 g TiO$_2$ powder was dispersed into 720 mL of deionized water for 30 min by ultrasound (360 W). Then, 100 mL anhydrous methanol was added. After the reaction solution was transferred to the photoreactor (Yuming, YM-GHX-II), N$_2$ (0.4 MPa, 40 mL/min) was injected and sealed the reactor to eliminate the influence of oxygen. Keep stirring, turn on the 500 W side-lit Hg lamp (74 mW/cm^2) to start irradiation reaction (i.). Then, turn off the lamp after 1 h irradiation and turn up the magnetic stirring speed. Finally, 10 mL of noble metal precursor solution was added at the rate of 0.5 mL/s in dark for 30 min. The reaction temperature kept at 13°C $\pm$ 2°C by circulating water during the whole process. The precipitation was collected by extraction and dried at 60°C for 8 h in air atmosphere. Finally, the sample powder was obtained after grinding.

Preparation of M(i.i.)/TiO$_2$ is shown in Figure S1C. In general, 0.3 g TiO$_2$ powder was dispersed into 720 mL deionized water for 30 min by ultrasound (360 W). Then, 100 mL anhydrous methanol was added. After the reaction solution was transferred to the photoreactor (Yuming, YM-GHX-II), N$_2$ (0.4 MPa, 40 mL/min) was injected and sealed the reactor was with sealing film to eliminate the influence of oxygen. Keep stirring, turn on the 500 W side-lit Hg lamp (74 mW/cm^2) to start irradiation reaction (i.). After the first step of irradiation for 30 min, 10 mL of noble metal precursor was added at the rate of 0.5 mL/s, and the second step of irradiation continued for 30 min. The reaction temperature kept at 13°C $\pm$ 2°C by circulating water during the whole process. The precipitation was collected by extraction and dried at 60°C for 8 h in air atmosphere. Finally, the final sample powder was obtained after grinding. Similarly, noble metals were deposited on other semiconductors (CeO$_2$, ZrO$_2$) by the same procedure.

The loading amounts of different noble metals are 2.5 wt.%. For the catalytic oxidation of HCHO, the different loading amounts have been denoted.

Catalytic performance test

Temperature programmed H$_2$ reduction (H$_2$-TPR) measurements were carried out by an automatic adsorption apparatus with TCD detector (AutoChem1 II 2920). The catalyst (0.1 g, 40–60 mesh) was placed in a quartz tube and heat treated for 1 h in a He flow at 300°C. After the catalyst cooled to 50°C, 5% H$_2$ (95% He) flow was injected until the baseline was stable. The desorption curve was obtained using TCD by elevating the temperature from 50°C to 700°C at a rate of 10°C/min.

In-situ diffuse reflectance infrared fourier transformed spectroscopy (DRIFTS) was carried out on TENSOR 27 spectroscope apparatus (Bruker), equipped with a diffuse reflectance accessory and a MCT detector. About 40 mg finely ground sample was packed *in situ* chamber with quartz observation window. 50 mL/min Ar or HCHO flow (50 ppm, Ar balance) and reactant stream (O$_2$ 20 vol%, Ar balance) was introduced. The spectra under reaction conditions were recorded after 64 scans with a resolution of 4 cm^{-1}.

The catalytic oxidation performance of HCHO was determined by the difference in the HCHO concentration of inlet and outlet when 200 ppm HCHO (gas consists of 200 ppm HCHO, 20 vol% O$_2$ and 80 vol%N$_2$) was injected into a fixed bed with 0.3 g catalyst at 25°C. The relative humidity is 40%. The total gas flow rate was 250 mL/min, gas hourly space velocity (GHSV) was 35,000 h^{-1}. The HCHO concentration in inlet and outlet gas was determined by acetylacetone spectrophotometry: 10 mL deionized water was used to collect the inlet and outlet HCHO mixture gas for 5 min 1 mL absorption solution was added into 11 mL of acetylacetone indicator and heated in a 100°C water bath for 5 min. After cooling to room temperature, the absorbance at 413nm was measured using a UV-Vis spectrophotometer. The concentration of HCHO was calculated according to Equation (1):

$$\text{HCHO conversion (\%)} = \frac{[\text{HCHO}]_{\text{inlet}} - [\text{HCHO}]_{\text{outlet}}}{[\text{HCHO}]_{\text{inlet}}} \times 100\% \qquad \text{(Equation 1)}$$

where: [HCHO]$_{\text{inlet}}$ is the concentration of HCHO while entering the gaseous mixture. [HCHO]$_{\text{outlet}}$ is the concentration of HCHO while exiting the gaseous mixture.

Methods for characterization

The morphology and size of the samples were characterized by high-resolution transmission electron microscopy (HRTEM, JEM-200CX). The X-ray power diffraction (XRD) was recorded on a Rigaku D/MAX2200V powder diffractometer using Cu-Kα radiation. UV-visible diffuse reflectance spectra (UV–Vis DRS) were recorded on a UV-vis spectrophotometer (UV-2600) equipped with a dual-beam UV-Vis spectrophotometer and $BaSO_4$ was used as a reflectance standard. The valence states of noble metals were analyzed by X-ray photoelectron spectroscopy (XPS). The φ-5000 C energy spectrum system was upgraded by RBD, and the Mg-Kα radiation as the excitation source at the base pressure of 5×10^{-9} mbar. All the binding energy (BE) spectra were calibrated with a C 1s line centered at 284.6 eV from contaminant carbon. The actual noble metal loading was determined by inductively coupled plasma emission spectroscopy (ICP, Jena PQ-9000, Germany). The electron paramagnetic resonance (EPR) spectra were recorded on a Bruker A300 EPR spectrometer at an X-band frequency of 9.852 GHz, sweep width of 300.00 Gauss, and center field of 3550.00 Gauss. The test samples were ultrasonically dispersed into the mixture of deionized water and methanol, placed in an in-situ cell, and then passed into N_2 (20 mL/min). Turn on the 100 W mercury lamp light and reacted for 1 h, then turn off the light source before collecting the initial signals. Then, Pt precursor aqueous solution was injected and recorded the signals at regular intervals.